



Catalytic transformation of microplastics to functional carbon for catalytic peroxyomonosulfate activation: Conversion mechanism and defect of scavenging



Shiying Ren ^a, Xin Xu ^a, Zhong-Shuai Zhu ^a, Yangyang Yang ^b, Wenjie Tian ^a, Kunsheng Hu ^a, Shuang Zhong ^a, Jiabao Yi ^c, Xiaoguang Duan ^{a,*}, Shaobin Wang ^{a,*}

^a School of Chemical Engineering, The University of Adelaide, Adelaide, SA 5005, Australia

^b Institute of Green Chemistry and Chemical Technology, School of Chemistry & Chemical Engineering, Jiangsu University, Zhenjiang 212013, China

^c Global Innovative Center for Advanced Nanomaterials, the University of Newcastle, Callaghan, NSW 2308, Australia

ARTICLE INFO

Keywords:

Plastics
Carbon nanosheets
Persulfate activation
Pollutant degradation
Radical scavengers

ABSTRACT

Plastic wastes were catalytically transformed into different structured carbons as effective catalysts for peroxyomonosulfate activation to degrade organic pollutants in water and the catalytic conversion mechanism was comprehensively investigated. A salt template-based carbonization approach was successfully developed to catalytically converting high-density polyethylene (HDPE) into diverse carbon materials, such as core-shell carbon composites, nanosheets, and their hybrids. The morphology and proportions of structure defective carbon were found to be controlled by a NiCl_2 to HDPE ratio. Carbon nanosheets performed excellent catalytic efficiency in peroxyomonosulfate activation toward phenol oxidation, due to a high content of reactive defects via a nonradical electron-transfer mechanism. More importantly, deliberate experiment design and kinetic analyses were employed to illustrate the artifact of radical scavengers (e.g., ethanol) in mechanistic investigation for nonradical/radical reaction. This work provides an upcycle approach for waste plastics into carbocatalysts and new insight to the conversion process and advanced water purification.

1. Introduction

Plastics were first invented in 1907 and have been extensively applied in packaging, construction, and textile industries [1]. Numerous plastic products are growing as an indispensable part of human life, and their production soared from 1.5 million tons in 1950–391 million tons in 2019 [2]. Millions of tons of plastics spread to almost every corner of the world and can be found in the land, ocean, air, and even in the organs of animals. Most plastics are persistent and durable due to the robust polymer structure and diverse chemical additives, making them hard to be decomposed in nature, and have posed a big threat to our ecosystem. Thus, extensive efforts have been made to reuse plastics and explore their transformation into value-added products, such as carbon nanotubes, graphene, and hydrocarbon products [3]. Particularly, plastics are carbon-rich materials and show huge potential in converting into carbon materials. In comparison, the gaseous products from fossil fuels (e.g., methane, ethylene, propylene) are normally used as precursors to produce carbon nanomaterials in traditional methods. The

processes are costly and non-renewable, limiting the large-scale fabrication of carbon nanomaterials for commercial applications.

In this regard, plastics are cheaper, with well-defined compositions and units, and easier to control carbonization processes [4,5]. Graphene [6], carbon nanotubes [7–11], carbon spheres [12,13], carbon nanosheets (CNSs) [14,15], and porous carbon [16–18] have been successfully produced from different plastics. For example, Jie et al. [19] directly transformed plastics (polyethylene, polypropylene, and polystyrene) to hydrogen and multi-wall carbon nanotubes in a microwave reactor. The global demand for carbon nanomaterials has been growing rapidly. Taking graphene for an example, its global market demand is ranging from US\$15–50 million in 2015 and will soar to US\$200–2000 million in 2025 [2]. These plastic-derived carbon nanomaterials have a wide range of applications, such as supercapacitors [20,21], batteries [22,23], gas/liquid storage or separation [24–26], and water remediation [27,28]. Therefore, converting waste plastics into high-value-added carbon/nanocarbon materials is promising in reducing the environmental hazards as well as accelerating the development of functional

* Corresponding authors.

E-mail addresses: xiaoguang.duan@adelaide.edu.au (X. Duan), shaobin.wang@adelaide.edu.au (S. Wang).

carbon materials.

With the development of industrialization, a diversity of organic contaminants, such as antibiotics, dyes, and additives, have been discharged into the freshwater systems. The deteriorated water quality poses a great threat to the health of human beings and other organisms. As a powerful water remediation technology, advanced oxidation processes (AOPs) can directly decompose organic pollutants into non-toxic compounds in water. While metal-based AOPs normally employ transition metals and metallic oxides as catalysts, which result in heavy metal leaching and thus secondary contamination to water systems [29]. Since the first utilization of reduced graphene oxides in peroxymonosulfate (PMS) activation was reported [30], persulfates have appealed huge interests as a result of the following advantages: 1) persulfates are convenient to store and transport as chemically stable solids; 2) a high oxidation potential and high yield of reactive oxygen species (ROS) leads to rapid degradation of diverse pollutants; 3) various methods (ultrasound, heat, ultraviolet light, chemicals, metals, and carbons) can be used to activate persulfates to initiate radical and nonradical oxidation pathways [31]. Specifically, nanocarbon materials have been extensively studied because of their advantageous features, such as metal-free nature, source abundance, and outstanding biocompatibility and activity/selectivity [32–34].

The catalytic efficiency of metal-free carbocatalysts in AOPs largely depends on their intrinsic structure (or carbon configuration), surface chemistry, and defect degrees. For instance, pure sp^3 hybridized nanodiamonds exhibit low activity in the activation of peroxydisulfate/PMS, whereas graphitized nanodiamonds with an sp^2 @ sp^3 hybrid structure exhibited enhanced catalytic efficiency [35]. The heteroatom doping of carbon such as nitrogen [36], sulfur [37], boron, and phosphorous [38] can create point defects in carbon matrixes and further elevate the catalytic performance. The oxygen groups in the carbon network could regulate the reductivity as well as the interaction with persulfate anions, thereby regulating the activity for organic oxidation [34]. Besides the above mentioned factors, amorphous carbon also has significant impacts on the carbon surface coordination environment and chemistry [39,40], however its impact on the catalytic activity in AOPs was less explored due to lacking a platform of model catalysts with controlled defects and graphitic degrees.

Polyethylene, the most widely consumed plastic in Europe at a staggering 13.7 million metric tons in 2021 [2], finds an extensive use in our daily life, primarily for bags, containers, and bottles. This ubiquitous material also contributes to the substantial volumes of waste polyethylene products generated globally each day. Nickel chloride is an effective catalyst to manufacture graphene-like materials [41]. Thereby in this study, we choose the high-density polyethylene (HDPE) as the carbon source and nickel chloride as the catalyst and template for plastic transformation and fabrication of a variety of nanocarbon materials and further investigate the conversion mechanism. The obtained core-shell structured carbon, hybrids, and CNSs were further explored to unravel the functions of graphitic and amorphous carbons in the activation of PMS and the associated oxidation pathways. Particularly, we investigated the impact of the dosage of alcohols as radical scavengers in nonradical systems, where their inhibition was typically misunderstood to be caused by radical scavenging. This work provides a promising pathway to transform HDPE into value-added carbon materials and catalytic application in organic-containing water decontamination with new insight on the processes.

2. Experimental section

2.1. Chemicals

Polyethylene (high density, melt index 12 g/10 min), nickel chloride hexahydrate ($NiCl_2$, ≥ 95 %), hydrochloric acid (HCl, 37 %), oxone (origin of PMS), phenol (≥ 99 %), cobalt sulfate heptahydrate ($CoSO_4$, ≥ 99 %), methanol (≥ 99.9 %), ethanol absolute (≥ 99.5 %), isopropanol

(≥ 99.9 %), tertiary butanol (≥ 99.5 %), 2,2,6,6-tetramethyl-4-piperidinol (98 %), 5,5-dimethyl-1-pyrrolidine N-oxide (≥ 97.0 %), nitrobenzene (≥ 99 %), atrazine (analytical standard), benzoic acid (≥ 99.5 %), salicylic acid (≥ 99 %), bisphenol A (BPA, ≥ 99 %), 4-hydroxybenzoic acid (≥ 97 %), naproxen (meets USP testing specifications), sulfamethoxazole (analytical standard), tetracycline hydrochloride (bioreagent), graphite (<45 μm , ≥ 99.99 %), activated charcoal Norit®, potassium iodide (KI, ≥ 99 %), and sodium bicarbonate ($NaHCO_3$, ≥ 99.7 %) were purchased from Sigma-Aldrich. Carbon nanotube (multi-walled, > 95 %) was purchased from Aladdin. Graphene flake was purchased from Nanjing Xianfeng Nanomaterial Technology Co., Ltd.

2.2. Synthesis of carbon nanomaterials from HDPE

HDPE was first chopped into small pieces with a blender. And then, $NiCl_2$ and HDPE pieces were added to 80 mL ethanol following the mass ratio as described in Table S1. Subsequently, the mixture was stirred at 70 °C until the ethanol was evaporated. The precipitate was ground into fine powder by mortar and pestle. The powder was placed into a tube furnace, annealed at 210 °C for 1 h, then heated to 800 °C, and maintained for 3 h. The heating process underwent in the nitrogen atmosphere, and the obtained carbon materials were ground and immersed in concentrated hydrochloric acid (20 %), stirring for 8 h to thoroughly remove nickel compounds. Then the solution was filtered and washed with ultrapure water and ethanol several times until the pH of the solution reached 7. The purified carbon materials were dried in an oven at 60 °C for two days and the dried carbon samples were named CS1, CS2, H3, H4, CNS5, and CNS6, respectively, according to the ratio of $NiCl_2$ and HDPE (1/10, 1/5, 1/1, 5/1, 10/1, 15/1).

2.3. Material characterizations

The morphologies of carbon samples were obtained by scanning electron microscopy (SEM, FEI Quanta 450) and transmission electron microscopy (TEM, Tecnai G2 Spirit 120k Volt). HAADF images and elemental mapping were conducted on the FEI Titan Themis 80–200. Raman spectra were carried out on a Raman spectrometer (Horiba LabRAM HR Evolution) with a green laser emitting at 532 nm. X-Ray diffraction (XRD) was performed on the Rigaku MiniFlex 600. The specific surface areas of the carbon samples were analyzed by the Brunauer–Emmett–Teller (BET) method from N_2 adsorption–desorption isotherms (Micromeritic ASAP2460). The Mettler Toledo was utilized to acquire the thermogravimetric analysis-differential scanning calorimetry (TGA–DSC) data for all carbon samples. Electron paramagnetic resonance (EPR) spectra using 5,5-dimethyl-1-pyrrolidine N-oxide and 2,2,6,6-tetramethyl-4-piperidinol as spin-trapping agents were conducted on a Bruker EMS-plus instrument.

2.4. Catalytic performance of plastic-derived carbon in AOPs

Initially, 10 ppm phenol or other organics was dissolved into 100 mL ultrapure water and the addition of 0.05 g L⁻¹ catalyst (carbon or other catalysts) followed. After the pre-adsorption for 30 min, 3 mM PMS was added and water samples were withdrawn periodically by a syringe with a 0.22 μm filter. All degradation tests were conducted at 25 °C under constant stirring of 800 rpm. The pseudo-first-order kinetic rate constants were computed by the following equation,

$$\ln(C/C_0) = -kt \quad (1)$$

Where, C_0 is the initial organic concentration, C is the organic concentration at time t , and k is the reaction rate constant.

The adsorption capacity (q_e , mmol g⁻¹) of organics was calculated by the following equation,

$$q_e = \frac{V(C_0 - C_t)}{m M} \quad (2)$$

Where, q_e is the adsorption capacity of organics, V is the volume of the reaction solution, C_0 is the initial organic concentration, C_t is the organic concentration at time t , m is the mass of the adsorbent, and M is the relative atomic mass of organics.

During the quenching tests, the radical scavengers were added after the organics but before the catalysts, and the other procedures were the same as the degradation tests. The dosage of scavengers was defined by the requirement of each test. The adsorption tests were performed to explore the impact of scavenger dosage on organics adsorption capacity. Their procedures were the same as quenching tests but without addition of PMS. The concentration of organics (excluding salicylic acid) was analyzed on an ultrahigh performance liquid chromatography (Ultimate 3000) with a C-18 column. Salicylic acid was analyzed on a UV-vis spectrophotometer (Agilent Technologies, Cary Series).

2.5. Electrochemical measurements

The open circuit potential test was conducted on a CHI760E electrochemical workstation. Carbon samples (4 mg) were mixed with 450 μL isopropanol, 500 μL water, and 50 μL Nafion® 117 to form a suspension liquid by sonication. Then the prepared sample was coated on the glassy carbon electrode, which was used as the working electrode. Meanwhile, a Pt wire was adopted as the counter electrode and an Ag/AgCl electrode was applied as the reference electrode.

2.6. TGA-DSC tests

The TGA-DSC tests were performed on a TGA instrument from Mettler Toledo. All samples were pyrolyzed at $10 \text{ }^{\circ}\text{C min}^{-1}$, but HDPE

was under a nitrogen flow while the carbon samples were under an air flow. The proportion of nickel, graphite, and amorphous carbon in plastic-derived carbon samples was calculated by the equations below,

$$C_{Ni} = \frac{m_e}{m_t} \times \frac{M_{Ni}}{M_{NiO}} \quad (3)$$

$$C_G = \frac{m_d - m_e}{m_t} \quad (4)$$

$$C_a = 1 - C_{Ni} - C_G \quad (5)$$

Where, C_{Ni} refers to the proportion of nickel, m_e is the final mass of samples, m_t is the initial mass of carbon samples, M_{Ni} and M_{NiO} are the relative atomic masses of nickel and nickel oxide, respectively, C_G is the proportion of graphite, m_d is the mass at the division point between the two peaks of graphite and amorphous carbon (as shown the dotted line in Fig. S7), and C_a is the proportion of amorphous carbon.

2.7. PMS adsorption tests

The concentration of PMS was evaluated by the iodometric method on a UV-vis spectrophotometer (Agilent Technologies, Cary Series). Initially, 3 mM PMS was dissolved into 100 mL ultrapure water and the specific amount of ethanol was added. Subsequently, the mixed solution was blended with 0.05 g L⁻¹ carbon materials and continued stirring for 60 min. At the beginning and end, 0.2 mL reaction solution was withdrawn and mixed with 0.3 g KI, 0.06 g NaHCO₃, and 2.8 mL H₂O₂, and then the mixture was analyzed on the UV-vis system at 319 nm.

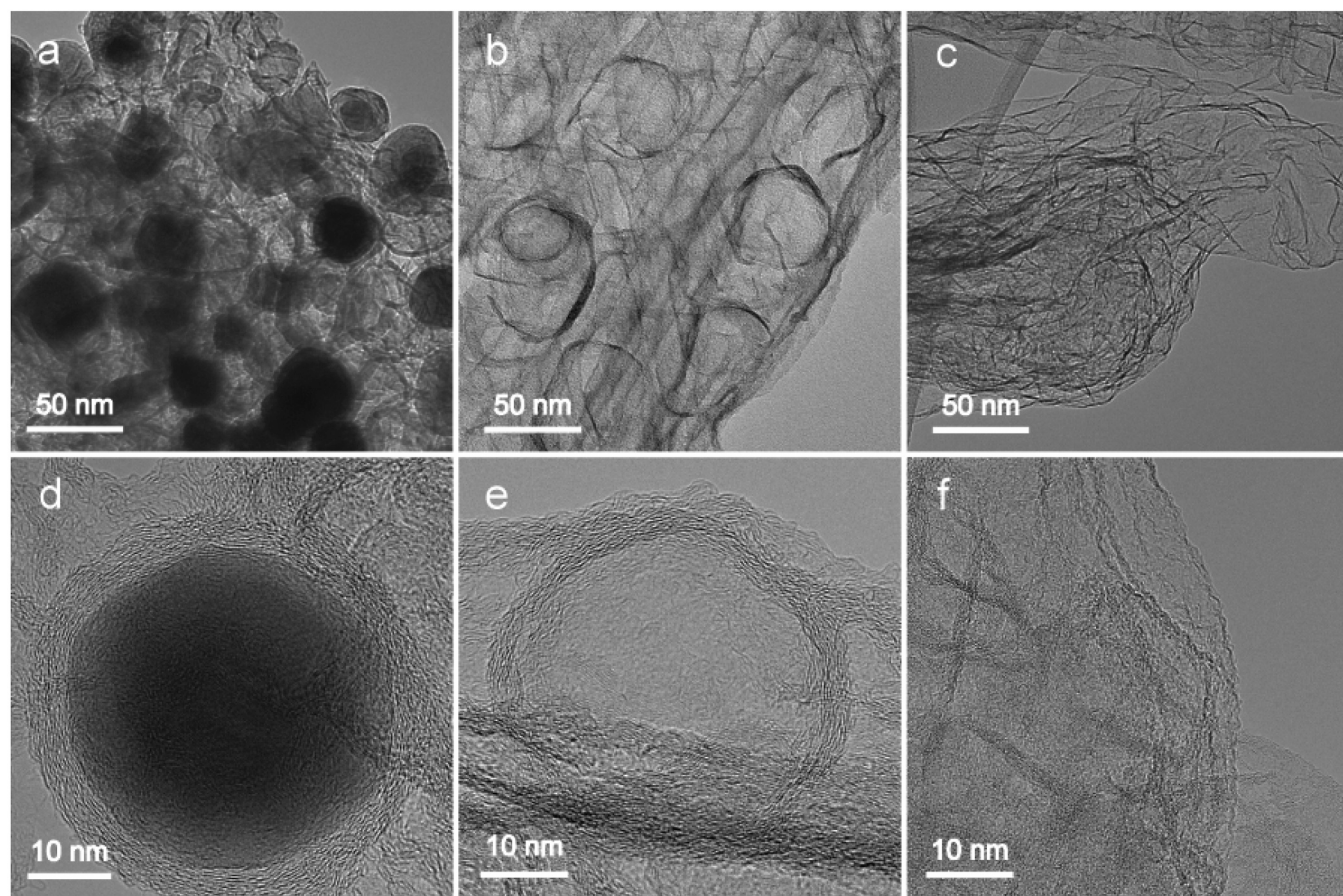


Fig. 1. TEM images of (a) CS1, (b) H3, (c) CNS6. HAADF images of (d) CS1, (e) H3, and (f) CNS6. Carbon samples, CS1, CS2, H3, H4, CNS5, and CNS6, were named according to the mass ratio of NiCl₂ and HDPE, 1/10, 1/5, 1/1, 5/1, 10/1, and 15/1, respectively.

3. Results and discussion

3.1. Formation mechanism of carbon materials

Figs. 1 and S1-S3 show that three types of carbons with different morphologies were obtained, including core-shell ($\text{Ni}@\text{C}$), CNSs, and their hybrid structures. The mass ratio of nickel chloride (NiCl_2) and HDPE is the key factor in controlling the carbon structures. With excessive HDPE (CS1 and CS2), $\text{Ni}@\text{C}$ will be formed (Fig. 1a, d, and S1). When NiCl_2 is excessive (CNS5 and CNS6), CNSs will be synthesized (Fig. 1b, f, and S2). In contrast, with similar loadings of HDPE and NiCl_2 (H3 and H4), a hybrid structure mixed with porous and lamellar carbons were fabricated (Fig. 1c, f, and S3). The spherical holes in the hybrid structure were generated by the removal of nickel particles using hydrochloric acid (Fig. 1b and e).

Fig. 2a manifests the XRD patterns of different carbon materials, and the sharp graphitic (002) peak at around $2\theta = 26^\circ$ suggests that CS1, CS2, H3, and H4 all contain graphitic carbons in high crystallinity, and the graphitic layers around nickel particles in Fig. 1d and e well supported the XRD results. In contrast, the broad (002) peak in CNS5 and CNS6 hints that they are composed of amorphous or graphene carbons.

The peaks at around 45° , 55° , and 77° correspond to the (111), (200), and (222) of metallic nickel, respectively, indicating that CS1, CS2, and H3 contain nickel particles, which can be observed in the SEM images (Fig. S1).

Fig. S4 shows the thermogravimetric analysis of HDPE under a N_2 atmosphere. HDPE underwent a rapid weight loss from 370 to 490 °C. During the process, HDPE was pyrolyzed into hydrogen and light hydrocarbons (e.g., methane, ethane, ethylene) [42], and these gaseous products reduced NiCl_2 to zero-valent nickel. The metallic nickel is a catalyst and can dissociate light hydrocarbons into carbon atoms, promoting the formation of a carbon network on the surface of nickel particles [43]. Therefore, when HDPE is excessive, all NiCl_2 will be reduced to metallic nickel, on which graphene layers are deposited to form $\text{Ni}@\text{C}$ composites (Fig. 2a), and protect the metallic core against acid pickling.

Fig. 2b shows the XRD patterns of NiCl_2 flakes, CNS6b (CNS6 before acid washing), and CNS6. NiCl_2 flakes were obtained by heating NiCl_2 up to 800 °C for three hours under a nitrogen atmosphere (Fig. S5a). It is easy to observe that CNS6b has both nickel and NiCl_2 peaks, but when CNS6b was purified by hydrochloric acid, only amorphous carbon (CNS6) was observed. Moreover, NiCl_2 flakes have similar

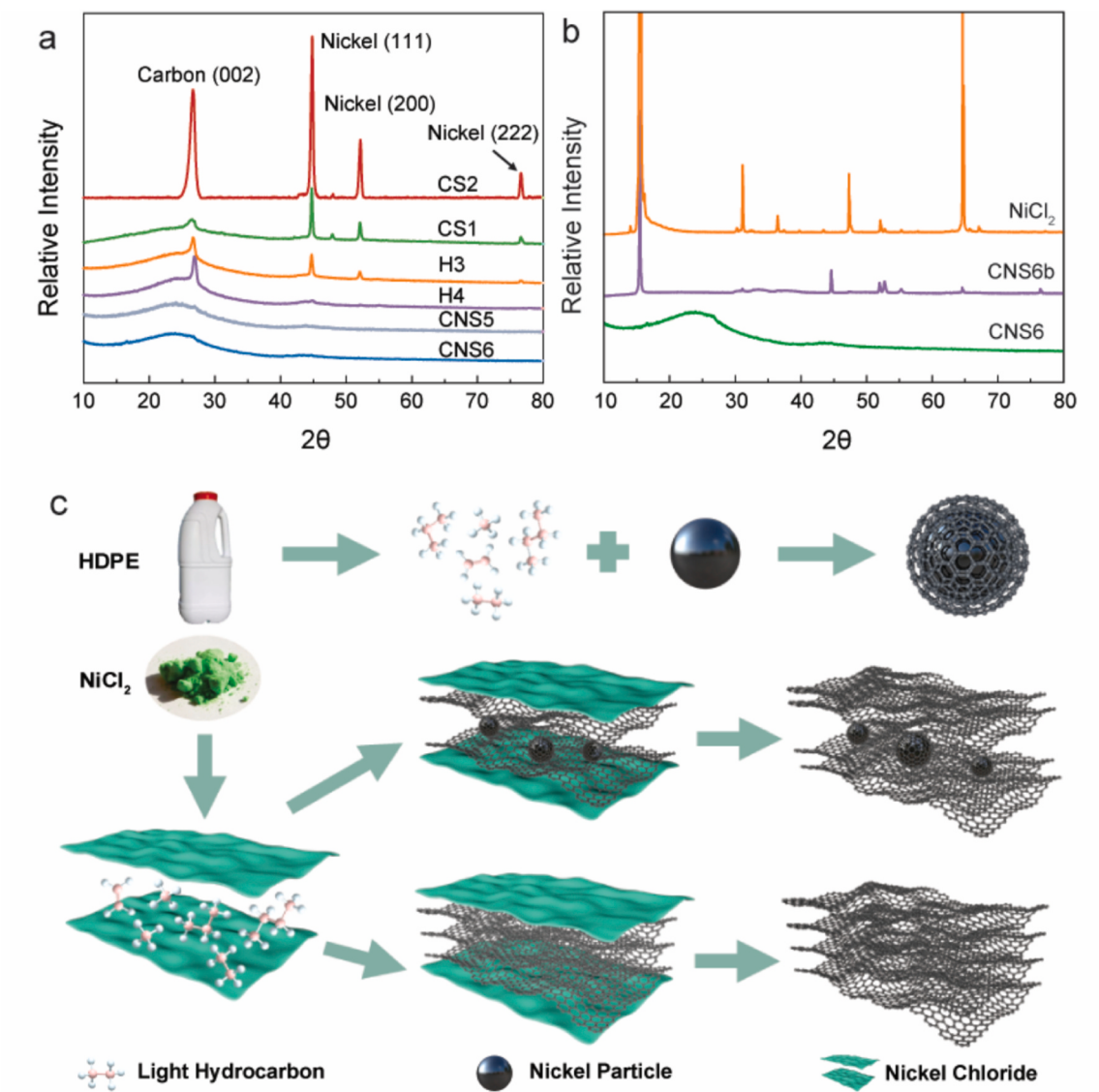


Fig. 2. XRD patterns of (a) CS1-CNS6 and (b) NiCl_2 flakes, CNS6b (CNS6 before acid washing), and CNS6. Schematic illustration of the formation of $\text{Ni}@\text{C}$ and CNSs (c).

microstructures to CNSs (Fig. S3b and S5b). It is reasonable to infer that, when HDPE is limited, only a small proportion of NiCl_2 will be reduced to nickel particles by the decomposed hydrocarbons, and the remaining NiCl_2 flakes will act as templates to facilitate the formation of CNSs under the high temperature (Fig. 2c). When HDPE is equal to NiCl_2 , the newly formed graphite cannot completely wrap up the nickel particles. Thus, the nickel particles are removed by the acid and spherical hollows are generated. Meanwhile, some carbon sheets are formed while NiCl_2 is lightly overdosed, forming the hybrid structure (intermediate state) with both Ni@C and CNSs.

Raman spectra of all carbon materials are applied to investigate the defective degree and structure distortion of all the samples, as depicted in Fig. 3a. The D band is well known as an indicator of the structural defects in the graphitic framework, while the G band is corresponding to the E_{2g} vibrational mode of the sp^2 -bonded graphitic carbons [44]. The intensity ratio of I_D/I_G is usually employed to manifest the population/degree of defects in carbonaceous materials. As shown in Fig. S6, the Raman spectra are further deconvoluted into five bands using Gaussian functions, assigned to D band (1342 cm^{-1}), G band (1574 cm^{-1}), D2 band (1272 cm^{-1}), D1 band (1465 cm^{-1}), and D' band (1613 cm^{-1}) [45]. Table S2 shows that the value of I_D/I_G increases from CS1 (0.49) to CNS6 (1.41), indicating the higher defect degree of CNSs than Ni@C . The ratio of $I_D/I_{D'}$ could identify the type of the defect in carbon nanomaterials, such as boundaries, vacancies or sp^3 carbons [46], and it could be calculated from the deconvolution of the first order Raman spectrum. Fig. 3b shows the $I_D/I_{D'}$ ratio for all samples, and their value between 1 and 2.5 suggests the boundaries are the primary defects

in all materials.

The specific surface areas (SSAs) of all samples were determined by nitrogen sorption tests using the Brunauer-Emmett-Teller (BET) approach, and are summarized in Table S2. The SSAs increase from CS1 ($78.5 \text{ m}^2 \text{ g}^{-1}$) to CNS6 ($1046 \text{ m}^2 \text{ g}^{-1}$), suggesting that the lamellar CNSs have a much larger SSA than Ni@C due to the 2D open structures. A dramatic difference between the two types of carbons is also observed in the nitrogen sorption isotherms in Fig. 3c. CNS6 has the IV-type isotherms with H3-type hysteresis loops while CS2 exhibits the II-type isotherms [41], which indicates that CNS6 has slit holes formed by the accumulation of layer structures and CS2 exhibits a non-porous structure.

The thermal stability of all samples (CS1-CNS6) in the air is analyzed by TG-DSC (Fig. S7). CS1 and CS2 have three oxidation peaks at 468, 558, and 650°C (Fig. S7a-7b), assigned to the oxidations of nickel particles, amorphous carbon, and graphitic carbon, respectively [47]. However, the nickel and graphitic carbon oxidation peaks are both weakened substantially for H3 and H4, but the amorphous carbon oxidation peak is still dominant (Fig. S7c-7d). As for CNS5 and CNS6, only one peak at 577°C (Fig. S7e-7f) appears, which suggests that the majority of CNSs is composed of amorphous carbons. The percentage of amorphous carbon is calculated based on DSC and TG analyses, and increases from 41.1 % (Ni@C) to 97.4 % (CNSs) in Table S2. The increase trend has a positive correlation with the dosage of NiCl_2 in the catalyst precursors (Table S1), which means NiCl_2 is a key role in the carbon structure formation processes. The results are consistent with the XRD analysis that, with the increase of NiCl_2 , the derived carbons

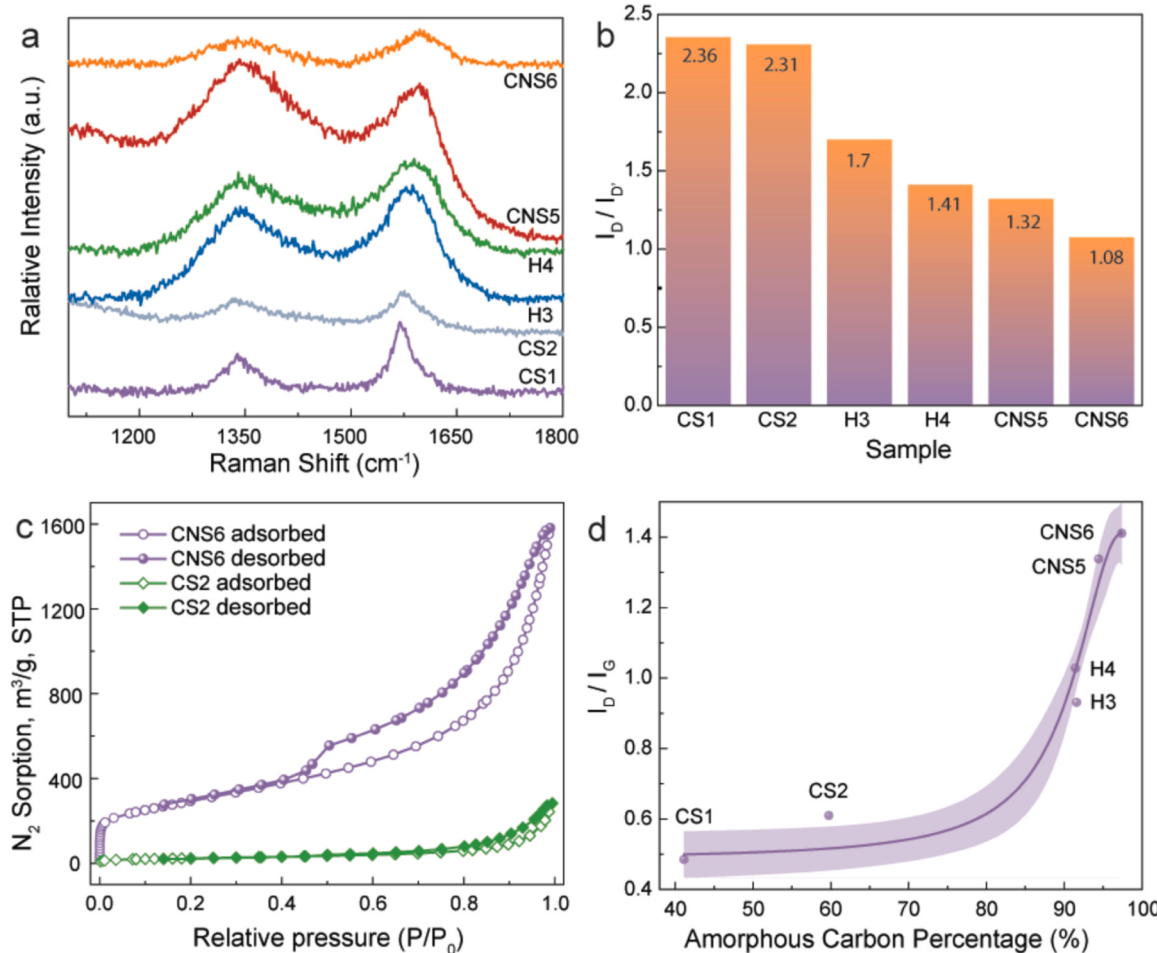


Fig. 3. (a) Raman spectra of different carbon samples. (b) The values of $I_D/I_{D'}$ for all samples. (c) The nitrogen sorption isotherms for CS2 and CNS6. (d) The relationship between amorphous carbon percentage and I_D/I_G ratio.

evolved from graphitic carbons to amorphous or graphene carbons due to the lack of metallic catalysts for graphitization, and the excessive NiCl_2 with sheet structure acted as templates to form the long-range disorder sheet carbons.

3.2. The role of defects and amorphous carbon in the activation of persulfates

The catalytic performances of all fabricated carbon materials in PMS activation for phenol removal are demonstrated in Fig. 4a. The $\text{Ni}@\text{C}$ samples (CS1 and CS2) show the lowest activity and decomposition of phenol at only 25 % in 90 min. CNSs (CNS5 and CNS6) exhibit the best catalytic performance and remove all phenol within 60 min. The different performances should be associated with the structure and physical properties of the carbon materials. Fig. S8 reveals that the I_D/I_G ratios increase with the SSAs as well as the carbon structure evolving from core-shell composites to CNSs. Integrated with Fig. 3b, we speculate that the rising I_D/I_G values may result from the fact that increasing NiCl_2 templates would create porous structures and more lattice boundaries, resulting in enlarged SSAs and populated edging defects.

It is well known that defect sites in carbon are not fully coordinated in structure and exhibit high chemical activity. They exhibit high chemical potentials and can break the homogeneity and inertness of a carbon network. Therefore, defects can activate oxidants and accelerate the associated redox processes to produce reactive species [32]. It is worth studying the relationship between defects and degradation efficiency. To exclude the impact of different SSAs on adsorption and catalytic processes, we normalized the pseudo-first-order kinetic rate constant (k_{obs}) of all samples by SSAs and the weight of catalyst (m_{catalyst}) to compare their intrinsic activity. Fig. 4b shows the nearly linear relationship between $k_{\text{obs}}/\text{SSA}/m_{\text{catalyst}}$ and I_D/I_G . The proportional relation indicates that the increasing number of boundary defects directly enhances the catalytic efficiency of carbon materials. In other words, the boundary defect sites of the HDPE-derived carbon contribute to PMS activation for phenol degradation.

Amorphous carbons are non-crystalline particles in the long range, but some short-range crystalline order can be observed. Amorphous carbons are normally associated with a large number of dangling bonds and mixed hybridizations with both sp^2 and sp^3 bonds. So it is thermodynamically metastable and can provide plentiful undercoordinated active sites for catalytic reactions [48]. As shown in Fig. 3d, the value of I_D/I_G has a sharp increase when the amorphous carbon percentage is higher than 90 %, which means the high proportion of amorphous carbon will dramatically increase the number of defects in carbon materials (CNS5 and CNS6). The defects in amorphous carbon are

sophisticated, because they might include carbon dots, particles, and even polymerized carbon chains with completely different sizes from molecular to nanometer/micrometer levels [39]. In general, the increase in the amorphous carbon percentage could constantly enhance the number of defects and further elevate the catalytic efficiency in AOPs.

3.3. Revealing the mechanism of the persulfate activation by carbon nanosheets

With the best catalytic performance, CNS6 was chosen to explore the mechanism for the activation of PMS during the degradation process. As shown in Fig. 5a, all scavengers (methanol, ethanol, isopropanol, and tertiary butanol) have no quenching effect on the degradation efficiency. Fig. S9a shows that phenol can be completely removed in 50 min in a CoSO_4/PMS system, but only 50 % phenol was removed in 90 min when ethanol (100 times compared to PMS) was added. The corresponding kinetic rate constant dramatically declined from 0.089 min^{-1} to 0.013 min^{-1} (Fig. S9b). CoSO_4/PMS is a typical radical oxidation system, and the scavenger has an obvious retardant effect on degradation processes. In comparison, phenol oxidized in the CNS6/PMS system should be via a nonradical pathway.

Chemical probing is another widely used method to identify free radicals [31]. Nitrobenzene and salicylic acid [49] are two chemical probes for hydroxyl radical ($\cdot\text{OH}$). Benzoic acid [50] and atrazine [51] are chemical probes for both sulfate ($\text{SO}_4^{\cdot-}$) and $\cdot\text{OH}$ radicals. Fig. 5b-d show that the addition of the catalyst has no positive impact on the degradation kinetics of the three probes in addition to the contribution by CNS6 adsorption. In addition, benzoic acid and salicylic acid can react with $\cdot\text{OH}$ to generate specific products of 4-hydroxybenzoic acid and dihydroxybenzoic acid, respectively. The two intermediates are not captured in Fig. 5d and e, further confirming a nonradical pathway of the CNS6/PMS system.

Moreover, EPR was adopted to inspect the generation of radical and singlet oxygen (${}^1\text{O}_2$) during the phenol degradation process. Generally, 5,5-dimethyl-1-pyrroline N-oxide (DMPO) is used to capture the short-lived $\text{SO}_4^{\cdot-}$ and $\cdot\text{OH}$ to form long-lived spin adducts. In the CNS6/PMS system, no $\text{SO}_4^{\cdot-}$ and $\cdot\text{OH}$ signals were detected (Fig. S10a). In addition, 2,2,6,6-tetramethyl-4-piperidinol (TEMP) is an effective capture agent for ${}^1\text{O}_2$, while the intensity of the three typical lines was not intensified by the addition of CNS6 (Fig. S10b), indicating that no ${}^1\text{O}_2$ was generated during the activation of PMS by CNS6. We also used TEMP as a scavenger of ${}^1\text{O}_2$ in the quenching test. The addition of TEMP does not show an obvious retarding effect on the degradation efficiency (Fig. S11). It proves that no ${}^1\text{O}_2$ is generated in the CNS6/PMS system.

According to the previous results, we speculate that PMS is activated

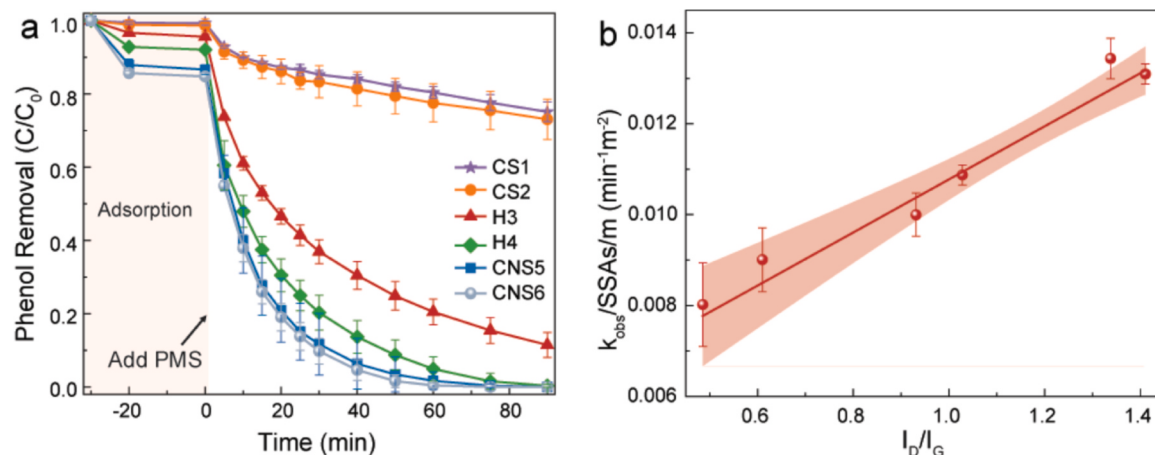


Fig. 4. (a) Phenol removal performances on various carbon materials (catalyst: 0.05 g L^{-1} , PMS: 3 mM , phenol: 10 ppm). (b) Correlation between I_D/I_G and kinetic rate constant.

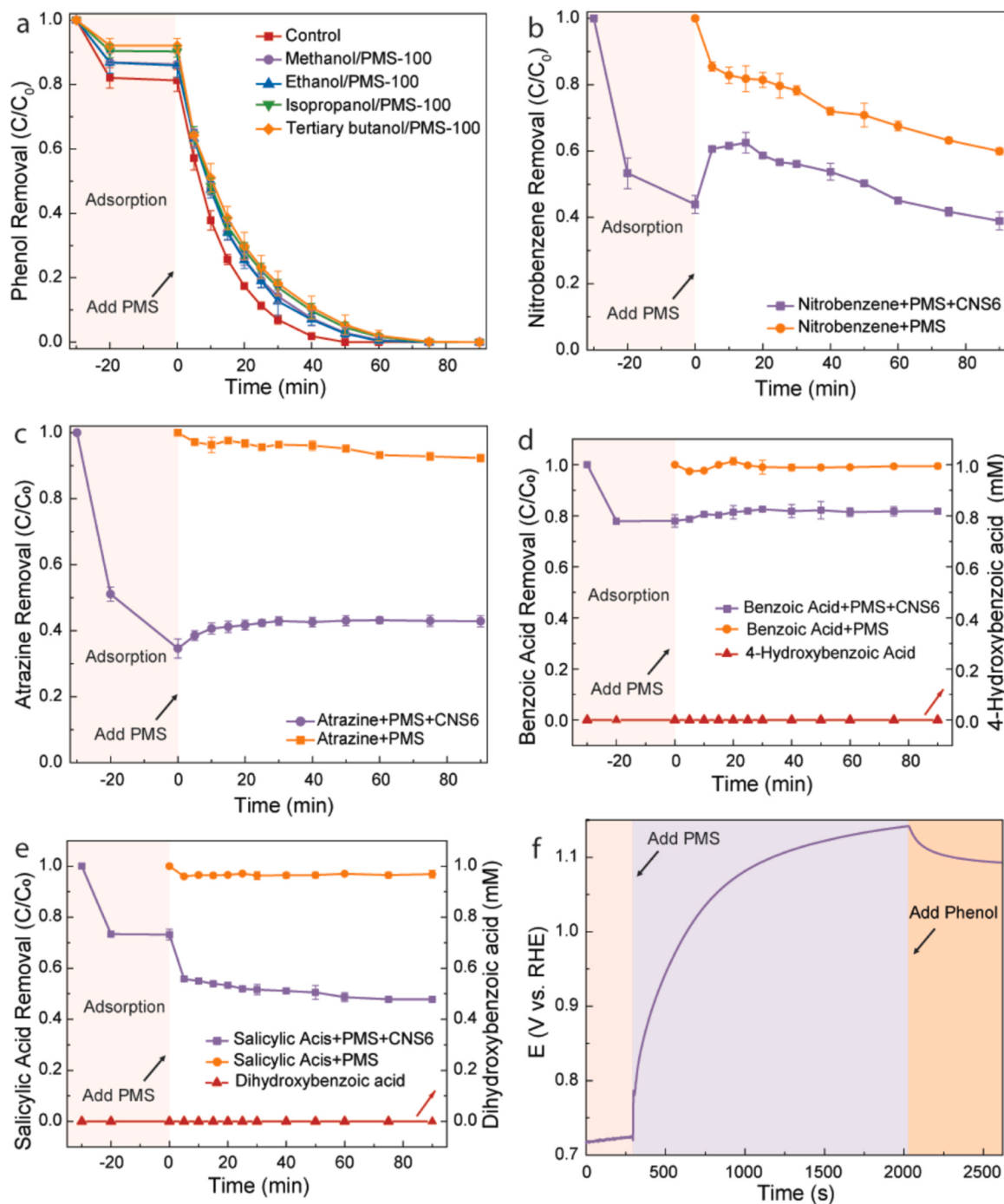


Fig. 5. (a) Quenching effect of different radical scavengers on phenol degradation by CNS6 (phenol: 10 ppm, PMS: 3 mM, CNS6: 0.05 g L^{-1}). The identification of free radicals by different chemical probes (chemical probe: 20 ppm, PMS: 3 mM, CNS6: 0.05 g L^{-1}), (b) nitrobenzene, (c) atrazine, (d) benzoic acid, and (e) salicylic acid. (f) Variation of open-circuit potentials for CNS6 electrode with addition of 3 mM PMS and 10 ppm phenol.

by CNS6 to realize organic oxidation via an electron-transfer pathway, which can be confirmed by the electrochemical tests (Fig. 5f, S12a, and S12b). Fig. 5f shows the stabilized potential of CNS6 in water is 0.72 V, which gradually goes up to 1.14 V in 30 min upon the addition of PMS, which should be caused by the activation of PMS. Electron transfer occurs from CNS6 to adsorbed PMS, forming a metastable CNS6/PMS^{*} complex that elevates the potential of carbon surface. Then a distinct drop in potential occurs when phenol (as the electron donor) is added. The reduction of potential should be due to the CNS6/PMS^{*} complex abstracting electrons from phenol and releasing the decomposed PMS [52]. During the redox process, CNS6 acts as both a

PMS activator and an electron shuttle to bridging phenol and PMS to coordinate electron migration and the subsequent redox reactions (PMS reduction into sulfate ions and phenol oxidation).

Furthermore, chronopotentiometry tests were also performed to certify the electron-transfer process during the oxidation. Fig. S12a shows that all currents approach zero irrespective of the presence of phenol at the equilibrium potential of + 0.72 V, because the applied potential was lower than the oxidation potential of PE (0.93 V) [53]. When the applied potential reached +1.14 V, the current with PE was much higher than that without PE, indicating that the presence of phenol (electron donor) will promote the electron-transfer process. In

the linear sweep voltammetry (LSV) tests (Fig. S12b), the lowest electrochemical current (-0.17 mA) was observed for the bare CNS6 electrode. When phenol or PMS is added separately, the currents increased to -0.2 mA and -0.26 mA accordingly, which should be due to the electron transfer occurred between phenol with CNS6 and PMS with CNS6. When phenol and PMS were added spontaneously, the highest current was achieved (-0.32 mA) and an obvious reduction peak appeared at 0.22 V, manifesting the rapid electron transfer from phenol to PMS on the surface of CNS6.

3.4. The impact of scavenger quantity on the adsorption and catalysis performance

In previous studies, quenching testing is a frequently applied technique for the judgement of catalytic pathway in AOPs. However, the quantity of scavengers in the quenching tests have a significant impact on reaction kinetics via affecting solution polarization, solubility, surface properties, and the interfacial interactions (e.g., adsorption and reaction). As demonstrated in Fig. 6a, with the increased dosage of ethanol addition, the degradation performance decreases dramatically. We observe that the additive amount of ethanol greatly influences the pollutant adsorption during the pre-adsorption process (Fig. S13). As shown in Fig. 6b, the increasing dosage of ethanol reduces the adsorption capacity of phenol. The adsorption capacity has a positive linear relationship with the kinetic rate constant (Fig. 6c), because organic adsorption on catalyst surface is critical in the electron-transfer regime. Therefore, the declined degradation performance in the presence of alcohols is attributed to the reduction of adsorption capacity rather than

the generation of radicals. Besides, Fig. 6d shows that the quantity of ethanol does not affect the PMS adsorption capacity, which further confirms the above conclusion.

In addition, the organic pollutant was changed with naproxen to probe whether it is a unique phenomenon or it is universal to other pollutants. In Fig. S14, a similar conclusion is obtained that the addition of ethanol decreased the adsorption capacity of naproxen and further weakened the degradation performances. Generally, this finding provides some insights into the alcohol quenching effects on determining radical/nonradical pathways in AOPs. For pollutants/persulfate with strong adsorption tendency to the catalyst, one should consider that the added quenching chemicals may affect the adsorption of reactants and reaction kinetics and thus prohibit the oxidation, giving rise to exaggerated contribution of radical pathways in mechanistic studies.

3.5. Environmental application

Fig. S15a is the comparison of naproxen adsorption between CNS6 and other commercial carbon materials, suggesting CNS6 shows the best adsorption performance. The degradation performance of CNS6 on various organic pollutants is also demonstrated in Fig. S15b. Except for 4-hydroxybenzoic acid, other organics are all completely removed in 40 min, indicating that CNS6 exhibits a universal removal capacity toward various organic pollutants. Fig. S16a shows the stability and reusability of CNS6/PMS oxidation system. About 100 % phenol is removed in 40 min in the first recycle, but only 50 % and 30 % of phenol are degraded in 90 min in the second and third runs, respectively. The deteriorated performance is partially resulted from the change in surface

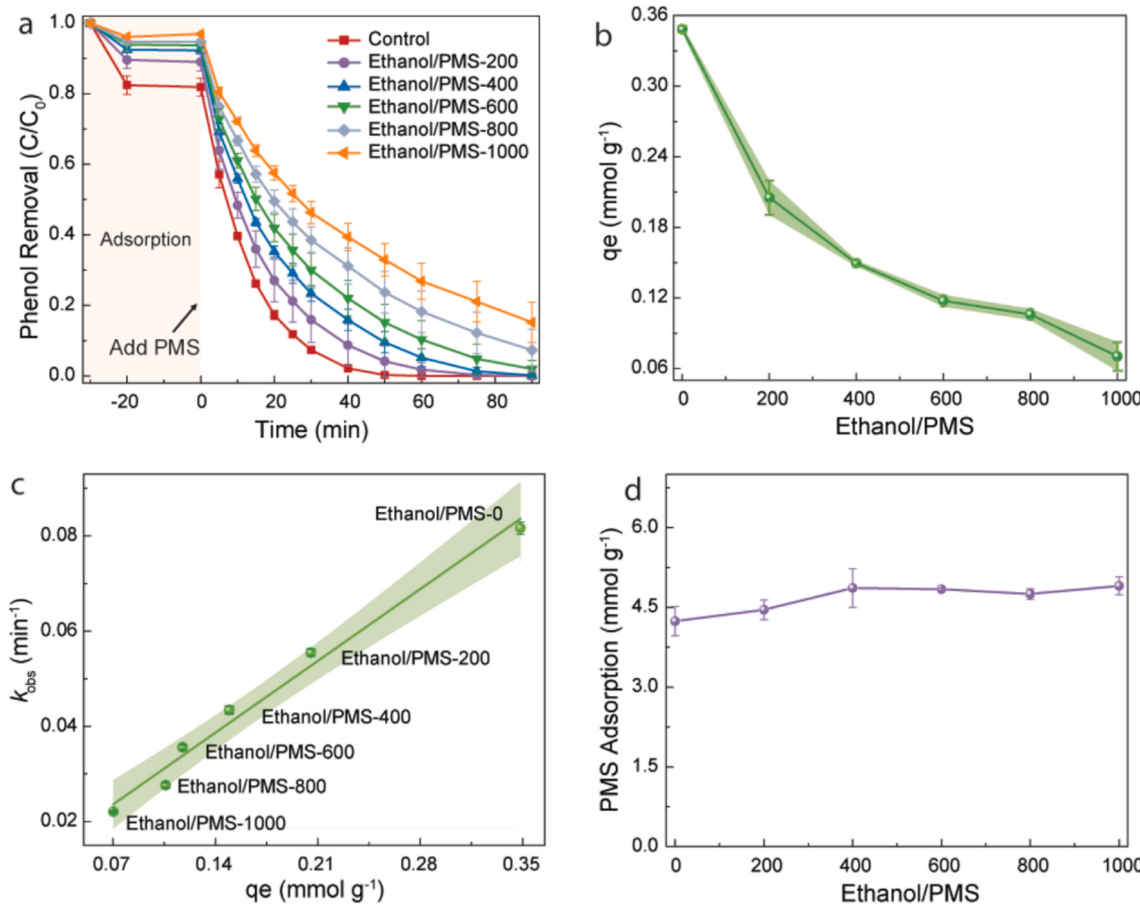


Fig. 6. (a) The impact of ethanol quantity on the catalysis performance of the CNS6/PMS oxidation system (phenol: 10 ppm, PMS: 3 mM, CNS6: 0.05 g L $^{-1}$). (b) Correlation of ethanol quantity and phenol adsorption capacity. (c) Correlation of phenol adsorption capacity and kinetic rate constant during the quenching test. (d) The impact of ethanol quantity on the PMS adsorption capacity (PMS: 3 mM, CNS6: 0.05 g L $^{-1}$).

chemistry of the carbocatalyst due to surface oxidation. Additionally, nonradical oxidation will initiate a polymerization pathway that converts phenol to polymeric products covering the surface of CNSs [54]. The coverage of active sites by intermediates will block their contact with PMS, leading to the deteriorated oxidation kinetics [55]. The catalytic performance of used samples can be recovered via re-pyrolysis at 800 °C for three hours under nitrogen atmosphere to remove the adsorbed phenol and polymeric intermediates.

Because natural water normally contains inorganic anions (such as Cl⁻, HCO₃⁻, HPO₄²⁻) and humic acid (HA), we investigated their influences on the degradation processes to assess the applicability of this system in natural water treatment. From Fig. S16b, we found that the addition of HA has some inhibition on phenol degradation, which may be caused by the competitive adsorption among HA, phenol, and PMS [41]. In addition, we found that the phenol removal efficiency slightly decayed from 100 % in ultrapure water to 94 % in the river water. The river water contains more natural organic matters which may compete with reactants for adsorption and phenol to react with the complex on the surface of CNS6. In contrast, anions of Cl⁻, HCO₃⁻, and HPO₄²⁻ have an inconspicuous effect on the degradation process, indicating that the nonradical-based CNS6/PMS system is promising to be applied for complex water remediation.

For the pilot-scale treatment of polluted water, a continuous flow system was assembled (Fig. 7a) to explore the applicability of CNS6 in the practical water purification scenarios. The CNS6 powders were uniformly dispersed on the cotton to make them contact the polluted water as much as possible during the purifying processes. The mixed solution of phenol and PMS flowed through the catalytic reactor from bottom to top to make sure they had sufficient reaction time to achieve the purification. The effluent was collected to track the residual phenol concentration. As shown in Fig. 7b, the system could attain a complete phenol removal in the first 1500 min at a flow rate of 1 mL/min, and then the degradation efficiency gradually declined due to the generation of polymeric byproducts covering the active sites of the catalysts. Such

deactivation is reversible, and the activity of catalysts could be retained after thermal pyrolysis (800 °C), which implicates that the CNSs material holds a great promise for practical applications in wastewater treatment.

The yields of different carbon materials from HDPE are summarized in Fig. S17. CNS1 obtains the least productivity (0.55 %), while CNS6 demonstrates the highest carbon yield (33.42 %). Thus, the carbon yield increases with the mass ratio of NiCl₂ to HDPE, indicating the critical role of NiCl₂ as both a catalyst and a template for plastic decomposition and re-constructing into template-directed carbonaceous materials with well-defined morphology and defective degrees. Therefore, the catalytic approach for plastic carbonization is of a low cost and attains a high carbon yield, which holds a great promise for the large-scale production of high-quality carbon composites and nanosheets. Particularly, the highly defective nature and open structure of CNSs hold great potential in applications for environmental catalysis and beyond.

4. Conclusion

In this work, we developed an efficient carbonization strategy for plastic carbonization into functional carbon materials with different structures and proportions of defective carbon using HDPE. In the process of synthesis, NiCl₂ acts as both a catalyst and a template for carbonization and subsequent morphology control. Carbon nanosheets demonstrate the best degradation performance for PMS activation and phenol removal in a nonradical manner. The catalytic efficiency of carbon nanosheets in AOPs exhibits a proportional relationship with the content of amorphous carbon, indicating that the structure defects are highly reactive in mediating PMS-based redox reactions. During the quenching tests, we found that the increased addition of ethanol was detrimental to the adsorption capacity of phenol and further impeded the degradation performance in the electron-transfer regime. This discovery clarified the cautious use of scavengers at a rational amount to avoid the misjudged (normally overestimated) radical contribution in

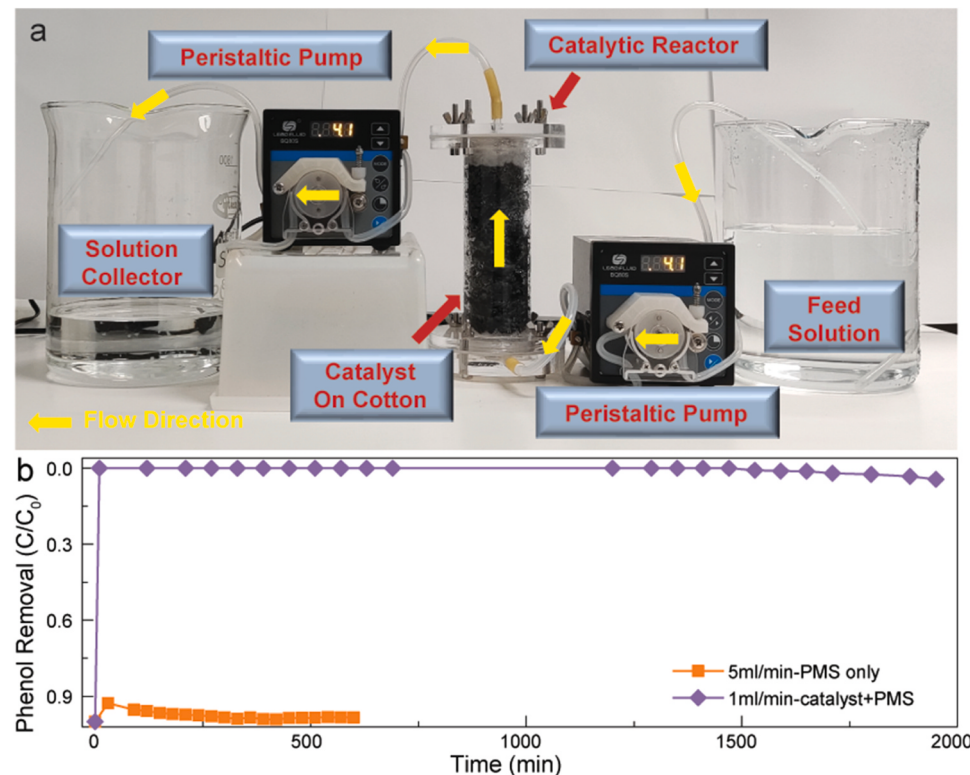


Fig. 7. (a) Photo of the pilot-scale water purification system. (b) The stability test of CNS6/PMS oxidation system. Reaction conditions: phenol = 5 mgL⁻¹, catalyst/CNS6 = 200 mg, T = 25 °C.

AOPs mechanism studies. In general, this study provides a promising method to transform plastics into value-added carbocatalysts with controlled morphology and molecular arrangement for advanced environmental remediation.

CRediT authorship contribution statement

Shiying Ren: Conceptualization, Investigation, Methodology, Formal analysis, Writing – original draft. **Xin Xu:** Investigation, Methodology, review, and editing. **Zhongshuai Zhu:** Investigation, Methodology. **Yangyang Yang:** Investigation, Methodology. **Wenjie Tian:** Investigation, Methodology. **Kunsheng Hu:** Investigation, Methodology. **Shuang Zhong:** Investigation, Methodology. **Jiabao Yi:** Investigation, Methodology. **Xiaoguang Duan:** Conceptualization, Investigation, Methodology, Writing – review and editing, Supervision. **Shaobin Wang:** Conceptualization, Investigation, Writing – review and editing, Supervision.

Declaration of Competing Interest

The authors declare that they have no known competing financial interests or personal relationships that could have appeared to influence the work reported in this paper.

Data Availability

Data will be made available on request.

Acknowledgements

We acknowledge the Australian Research Council for the financial support (DP200103206, LP200201079, DE210100253 and DE220101074). We also thank Hongyu Zhou and Peng Zhou for the analyses of the Brunauer-Emmett-Teller (BET) based SSA and porous structures.

Appendix A. Supporting information

Supplementary data associated with this article can be found in the online version at [doi:10.1016/j.apcatb.2023.123410](https://doi.org/10.1016/j.apcatb.2023.123410).

References

- [1] R. Geyer, J.R. Jambeck, K.L. Law, Production, use, and fate of all plastics ever made, *Sci. Adv.* 3 (2017) 25–29, <https://doi.org/10.1126/sciadv.1700782>.
- [2] PlasticEurope, Plastics – the Facts 2022, (2022). (<https://plasticseurope.org/knowledge-hub/plastics-the-facts-2022/>).
- [3] W. Tian, P. Song, H. Zhang, X. Duan, Y. Wei, H. Wang, S. Wang, Microplastic materials in the environment: problem and strategical solutions, *Prog. Mater. Sci.* 132 (2023), 101035, <https://doi.org/10.1016/j.jpmatsci.2022.101035>.
- [4] S. Ren, X. Xu, K. Hu, W. Tian, X. Duan, J. Yi, S. Wang, Structure-oriented conversions of plastics to carbon nanomaterials, *Carbon Res.* 1 (2022) 15, <https://doi.org/10.1007/s44246-022-00016-2>.
- [5] J. Gong, X. Chen, T. Tang, Recent progress in controlled carbonization of (waste) polymers, *Prog. Polym. Sci.* 94 (2019) 1–32, <https://doi.org/10.1016/j.progpolymsci.2019.04.001>.
- [6] L. Cui, X. Wang, N. Chen, B. Ji, L. Qu, Trash to treasure: converting plastic waste into a useful graphene foil, *Nanoscale* 9 (2017) 9089–9094, <https://doi.org/10.1039/c7nr03580b>.
- [7] C. Zhuo, B. Hall, H. Richter, Y. Levendis, Synthesis of carbon nanotubes by sequential pyrolysis and combustion of polyethylene, *Carbon* 48 (2010) 4024–4034, <https://doi.org/10.1016/j.carbon.2010.07.007>.
- [8] X. Wen, X. Chen, N. Tian, J. Gong, J. Liu, M.H. Rümmeli, P.K. Chu, E. Mijowska, T. Tang, Nanosized carbon black combined with Ni₂O₃ as “universal” catalysts for synergistically catalyzing carbonization of polyolefin wastes to synthesize carbon nanotubes and application for supercapacitors, *Environ. Sci. Technol.* 48 (2014) 4048–4055, <https://doi.org/10.1021/es404646e>.
- [9] J. Gong, J. Liu, L. Ma, X. Wen, X. Chen, D. Wan, H. Yu, Z. Jiang, E. Borowiak-Palen, T. Tang, Effect of Cl/Ni molar ratio on the catalytic conversion of polypropylene into Cu-Ni/C composites and their application in catalyzing “Click” reaction, *Appl. Catal. B Environ.* 117–118 (2012) 185–193, <https://doi.org/10.1016/j.apcatb.2012.01.015>.
- [10] D. Yao, H. Li, B.C. Mohan, A.K. Prabhakar, Y. Dai, C.H. Wang, Conversion of waste plastic packings to carbon nanomaterials: investigation into catalyst material, waste type, and product applications, *ACS Sustain. Chem. Eng.* 10 (2022) 1125–1136, <https://doi.org/10.1021/acssuschemeng.1c05945>.
- [11] A. Veksha, M.Z. Bin Mohamed Amrad, W.Q. Chen, D.K. Binte Mohamed, S. B. Tiwari, T. Lim, G. Lisak, Tailoring Fe₂O₃–Al₂O₃ catalyst structure and activity via hydrothermal synthesis for carbon nanotubes and hydrogen production from polyolefin plastics, *Chemosphere* 297 (2022), 134148, <https://doi.org/10.1016/j.chemosphere.2022.134148>.
- [12] H. Zhang, X.-L. Zhou, L.-M. Shao, F. Lü, P.-J. He, Hierarchical porous carbon spheres from low-density polyethylene for high-performance supercapacitors, *ACS Sustain. Chem. Eng.* 7 (2019) 3801–3810, <https://doi.org/10.1021/acssuschemeng.8b04539>.
- [13] V.G. Pol, J. Wen, K.C. Lau, S. Callear, D.T. Bowron, C.K. Lin, S.A. Deshmukh, S. Sankaranarayanan, L.A. Curtiss, W.I.F. David, D.J. Miller, M.M. Thackeray, Probing the evolution and morphology of hard carbon spheres, *Carbon* 68 (2014) 104–111, <https://doi.org/10.1016/j.carbon.2013.10.059>.
- [14] J. Gong, J. Liu, X. Chen, Z. Jiang, X. Wen, E. Mijowska, T. Tang, Converting real-world mixed waste plastics into porous carbon nanosheets with excellent performance in the adsorption of an organic dye from wastewater, *J. Mater. Chem. A* 3 (2015) 341–351, <https://doi.org/10.1039/c4ta05118a>.
- [15] J. Gong, J. Liu, X. Wen, Z. Jiang, X. Chen, E. Mijowska, T. Tang, Upcycling waste polypropylene into graphene flakes on organically modified montmorillonite, *Ind. Eng. Chem. Res.* 53 (2014) 4173–4181, <https://doi.org/10.1021/ie4043246>.
- [16] C. Ma, J. Min, J. Gong, X. Liu, X. Mu, X. Chen, T. Tang, Transforming polystyrene waste into 3D hierarchically porous carbon for high-performance supercapacitors, *Chemosphere* 253 (2020), 126755, <https://doi.org/10.1016/j.chemosphere.2020.126755>.
- [17] W.A. Algozeeb, P.E. Savas, Z. Yuan, Z. Wang, C. Kittrell, J.N. Hall, W. Chen, P. Bollini, J.M. Tour, Plastic waste product captures carbon dioxide in nanometer pores, *ACS Nano* (2022), <https://doi.org/10.1021/acsnano.2c00955>.
- [18] J. Min, X. Wen, T. Tang, X. Chen, K. Huo, J. Gong, J. Azadmanjiri, C. He, E. Mijowska, A general approach towards carbonization of plastic waste into a well-designed 3D porous carbon framework for super lithium-ion batteries, *Chem. Commun.* 56 (2020) 9142–9145, <https://doi.org/10.1039/d0cc03236k>.
- [19] X. Jie, W. Li, D. Slocombe, Y. Gao, I. Banerjee, S. Gonzalez-Cortes, B. Yao, H. AlMegren, S. Alshihri, J. Dilworth, J. Thomas, T. Xiao, P. Edwards, Microwave-initiated catalytic deconstruction of plastic waste into hydrogen and high-value carbons, *Nat. Catal.* 3 (2020) 902–912, <https://doi.org/10.1039/s41929-020-00518-5>.
- [20] I. Yang, J. Yoo, D. Kwon, D. Choi, M.-S. Kim, J.C. Jung, Improvement of a commercial activated carbon for organic electric double-layer capacitors using a consecutive doping method, *Carbon* 160 (2020) 45–53, <https://doi.org/10.1016/j.carbon.2020.01.024>.
- [21] H. Yang, S. Kannappan, A.S. Pandian, J.-H. Jang, Y.S. Lee, W. Lu, Graphene supercapacitor with both high power and energy density, *Nanotechnology* 28 (2017), 445401, <https://doi.org/10.1088/1361-6528/aa8948>.
- [22] F.J. Sonia, M. Aslam, A. Mukhopadhyay, Understanding the processing-structure-performance relationship of graphene and its variants as anode material for Li-ion batteries: a critical review, *Carbon* 156 (2020) 130–165, <https://doi.org/10.1016/j.carbon.2019.09.026>.
- [23] J.-Y. Hwang, S.-T. Myung, Y.-K. Sun, Sodium-ion batteries: present and future, *Chem. Soc. Rev.* 46 (2017) 3529–3614, <https://doi.org/10.1039/C6CS00776G>.
- [24] Y.-J. Fu, C.-C. Hu, D.-W. Lin, H.-A. Tsai, S.-H. Huang, W.-S. Hung, K.-R. Lee, J.-Y. Lai, Adjustable microstructure carbon molecular sieve membranes derived from thermally stable polyetherimide/polyimide blends for gas separation, *Carbon* 113 (2017) 10–17, <https://doi.org/10.1016/j.carbon.2016.11.026>.
- [25] J. Gong, H. Lin, K. Grygiel, J. Yuan, Main-chain poly(ionic liquid)-derived nitrogen-doped micro/mesoporous carbons for CO₂ capture and selective aerobic oxidation of alcohols, *Appl. Mater. Today* 7 (2017) 159–168, <https://doi.org/10.1016/j.apmt.2017.02.009>.
- [26] W. Xing, C. Liu, Z. Zhou, L. Zhang, J. Zhou, S. Zhuo, Z. Yan, H. Gao, G. Wang, S. Z. Qiao, Superior CO₂ uptake of N-doped activated carbon through hydrogen-bonding interaction, *Energy Environ. Sci.* 5 (2012) 7323, <https://doi.org/10.1039/c2ee21653a>.
- [27] Q. Liu, Y. Pan, Q. Cao, B. Peng, F. Meng, S. Wang, R. Hong, Y. Shen, H. Zhang, Upcycling waste plastics into FeNi@CNTs’ chainmail catalysts for effective degradation of norfloxacin: The synergy between metal core and CNTs shell, *Sep. Purif. Technol.* 326 (2023), 124735, <https://doi.org/10.1016/j.seppur.2023.124735>.
- [28] J. Gong, J. Liu, X. Chen, Z. Jiang, X. Wen, E. Mijowska, T. Tang, One-pot synthesis of core/shell Co@C spheres by catalytic carbonization of mixed plastics and their application in the photo-degradation of Congo red, *J. Mater. Chem. A* 2 (2014) 7461–7470, <https://doi.org/10.1039/C4TA00173G>.
- [29] G.P. Anipsitakis, D.D. Dionysiou, Radical generation by the interaction of transition metals with common oxidants, *Environ. Sci. Technol.* 38 (2004) 3705–3712, <https://doi.org/10.1021/es035121o>.
- [30] H. Sun, S. Liu, G. Zhou, H.M. Ang, M.O. Tadé, S. Wang, Reduced graphene oxide for catalytic oxidation of aqueous organic pollutants, *ACS Appl. Mater. Interfaces* 4 (2012) 5466–5471, <https://doi.org/10.1021/am301372d>.
- [31] X. Chen, W. Da Oh, T.T. Lim, Graphene- and CNTs-based carbocatalysts in persulfates activation: material design and catalytic mechanisms, *Chem. Eng. J.* 354 (2018) 941–976, <https://doi.org/10.1016/j.cej.2018.08.049>.
- [32] X. Duan, H. Sun, S. Wang, Metal-free carbocatalysis in advanced oxidation reactions, *Acc. Chem. Res.* 51 (2018) 678–687, <https://doi.org/10.1021/acs.accounts.7b00535>.

[33] J. Kang, L. Zhou, X. Duan, H. Sun, S. Wang, Catalytic degradation of antibiotics by metal-free catalysis over nitrogen-doped graphene, *Catal. Today* 357 (2020) 341–349, <https://doi.org/10.1016/j.cattod.2018.12.002>.

[34] W. Ren, L. Xiong, G. Nie, H. Zhang, X. Duan, S. Wang, Insights into the electron-transfer regime of peroxydisulfate activation on carbon nanotubes: the role of oxygen functional groups, *Environ. Sci. Technol.* 54 (2020) 1267–1275, <https://doi.org/10.1021/acs.est.9b06208>.

[35] X. Duan, C. Su, L. Zhou, H. Sun, A. Suvorova, T. Odedairo, Z. Zhu, Z. Shao, S. Wang, Surface controlled generation of reactive radicals from persulfate by carbocatalysis on nanodiamonds, *Appl. Catal. B Environ.* 194 (2016) 7–15, <https://doi.org/10.1016/j.apcatb.2016.04.043>.

[36] X. Duan, H. Sun, Y. Wang, J. Kang, S. Wang, N-doping-induced nonradical reaction on single-walled carbon nanotubes for catalytic phenol oxidation, *ACS Catal.* 5 (2015) 553–559, <https://doi.org/10.1021/cs5017613>.

[37] X. Duan, K. O'Donnell, H. Sun, Y. Wang, S. Wang, Sulfur and nitrogen co-doped graphene for metal-free catalytic oxidation reactions, *Small* 11 (2015) 3036–3044, <https://doi.org/10.1002/smll.201403715>.

[38] X. Duan, S. Indrawirawan, H. Sun, S. Wang, Effects of nitrogen-, boron-, and phosphorus-doping or codoping on metal-free graphene catalysis, *Catal. Today* 249 (2015) 184–191, <https://doi.org/10.1016/j.cattod.2014.10.005>.

[39] Y. Ding, Z.A. Qiao, Carbon surface chemistry: new insight into the old story, *Adv. Mater.* 34 (2022), 2206025, <https://doi.org/10.1002/adma.202206025>.

[40] F. Herold, S. Prosch, N. Oefner, K. Brunnengräber, O. Leubner, Y. Hermans, K. Hofmann, A. Drochner, J.P. Hofmann, W. Qi, B.J.M. Etzold, Nanoscale hybrid amorphous/graphitic carbon as key towards next-generation carbon-based oxidative dehydrogenation catalysts, *Angew. Chem. Int. Ed.* 60 (2021) 5898–5906, <https://doi.org/10.1002/anie.202014862>.

[41] J. Kang, H. Zhang, X. Duan, H. Sun, X. Tan, S. Wang, Nickel in hierarchically structured nitrogen-doped graphene for robust and promoted degradation of antibiotics, *J. Clean. Prod.* 218 (2019) 202–211, <https://doi.org/10.1016/j.jclepro.2019.01.323>.

[42] N. Cai, X. Li, S. Xia, L. Sun, J. Hu, P. Bartocci, F. Fantozzi, P.T. Williams, H. Yang, H. Chen, Pyrolysis-catalysis of different waste plastics over Fe/Al₂O₃ catalyst: High-value hydrogen, liquid fuels, carbon nanotubes and possible reaction mechanisms, *Energy Convers. Manag.* 229 (2021), 113794, <https://doi.org/10.1016/j.enconman.2020.113794>.

[43] J.P. Tessonnier, D.S. Su, Recent progress on the growth mechanism of carbon nanotubes: a review, *ChemSusChem* 4 (2011) 824–847, <https://doi.org/10.1002/cssc.201100175>.

[44] X. Xie, J. Long, J. Xu, L. Chen, Y. Wang, Z. Zhang, X. Wang, Nitrogen-doped graphene stabilized gold nanoparticles for aerobic selective oxidation of benzylic alcohols, *RSC Adv.* 2 (2012) 12438–12446, <https://doi.org/10.1039/c2ra21291a>.

[45] Q. Yang, Y. Chen, X. Duan, S. Zhou, Y. Niu, H. Sun, L. Zhi, S. Wang, Unzipping carbon nanotubes to nanoribbons for revealing the mechanism of nonradical oxidation by carbocatalysis, *Appl. Catal. B Environ.* 276 (2020), <https://doi.org/10.1016/j.apcatb.2020.119146>.

[46] A. Eckmann, A. Felten, A. Mishchenko, L. Britnell, R. Krupke, K.S. Novoselov, C. Casiraghi, Probing the nature of defects in graphene by Raman spectroscopy, *Nano Lett.* 12 (2012) 3925–3930, <https://doi.org/10.1021/nl300901a>.

[47] Y. Zhang, C. Wu, M.A. Nahil, P. Williams, Pyrolysis–catalytic reforming/gasification of waste tires for production of carbon nanotubes and hydrogen, *Energy Fuels* 29 (2015) 3328–3334, <https://doi.org/10.1021/acs.energyfuels.5b00408>.

[48] A. Kouchi, Amorphous carbon, in: *Encycl. Astrobiol.*, Springer, Berlin, Heidelberg, 2011, pp. 41–42, https://doi.org/10.1007/978-3-642-11274-4_70.

[49] H. Li, Q. Wang, Evaluation of free hydroxyl radical scavenging activities of some Chinese herbs by capillary zone electrophoresis with amperometric detection, *Anal. Bioanal. Chem.* 378 (2004) 1801–1805, <https://doi.org/10.1007/s00216-004-2509-1>.

[50] H. Lee, H. Il Kim, S. Weon, W. Choi, Y.S. Hwang, J. Seo, C. Lee, J.H. Kim, Activation of persulfates by graphitized nanodiamonds for removal of organic compounds, *Environ. Sci. Technol.* 50 (2016) 10134–10142, <https://doi.org/10.1021/acs.est.6b02079>.

[51] Z.H. Xie, C.S. He, H.Y. Zhou, L.L. Li, Y. Liu, Y. Du, W. Liu, Y. Mu, B. Lai, Effects of molecular structure on organic contaminants' degradation efficiency and dominant ROS in the advanced oxidation process with multiple ROS, *Environ. Sci. Technol.* 56 (2022) 8784–8795, <https://doi.org/10.1021/acs.est.2c00464>.

[52] W. Ren, C. Cheng, P. Shao, X. Luo, H. Zhang, S. Wang, X. Duan, Origins of electron-transfer regime in persulfate-based nonradical oxidation processes, *Environ. Sci. Technol.* 56 (2022) 78–97, <https://doi.org/10.1021/acs.est.1c05374>.

[53] W. Tian, J. Lin, H. Zhang, X. Duan, H. Sun, H. Wang, S. Wang, Enhanced removals of micropollutants in binary organic systems by biomass derived porous carbon/peroxymonosulfate, *J. Hazard. Mater.* 408 (2021), 124459, <https://doi.org/10.1016/j.jhazmat.2020.124459>.

[54] J. Dou, Y. Tang, Z. Lu, G. He, J. Xu, Y. He, Neglected but efficient electron utilization driven by biochar-co-activated phenols and peroxydisulfate: Polyphenol accumulation rather than mineralization, *Environ. Sci. Technol.* 57 (2023) 5703–5713, <https://doi.org/10.1021/acs.est.3c00022>.

[55] J. Kang, X. Duan, C. Wang, H. Sun, X. Tan, M.O. Tade, S. Wang, Nitrogen-doped bamboo-like carbon nanotubes with Ni encapsulation for persulfate activation to remove emerging contaminants with excellent catalytic stability, *Chem. Eng. J.* 332 (2018) 398–408, <https://doi.org/10.1016/j.cej.2017.09.102>.